Engineering 48 (2025) 205–219

Contents lists available at ScienceDirect

Engineering

journal homepage: www.elsevier.com/locate/eng

Research
Environmental Engineering—Article

Solar-Driven Dehydration and Purification of Oily Pollutants with a Multifunctional Biomass-based Carbon Aerogel: A Potential Step Towards Carbon Reduction

Fawei Lin [a], Hongyun Yao [a], Chujun Luan [a], Chenxu Zhong [a], Huiyi Mao [a], Lei Che [b], Hongdi Yu [a], Guanyi Chen [a,c,*], Eslam Salama [d], Mona Ossman [d], Li'an Hou [e,*]

[a] School of Environmental Science and Engineering, Tianjin Key Lab of Biomass Wastes Utilization, Tianjin University, Tianjin 300072, China
[b] College of Engineering, Huzhou University, Huzhou 313000, China
[c] School of Mechanical Engineering, Tianjin University of Commerce, Tianjin 300134, China
[d] Environment and Natural Materials Research Institute (ENMRI), Alexandria 21934, Egypt
[e] School of Environment, Beijing Normal University, Beijing 100875, China

ARTICLE INFO

Article history:
Received 9 July 2024
Revised 21 November 2024
Accepted 16 January 2025
Available online 27 January 2025

Keywords:
Solar photothermal utilization
Oily sludge
Biomass carbon aerogel
Pyrolysis
Carbon reduction

ABSTRACT

Efficient disposal of oily water pollution and oily sludge (OS) production with low energy demand has garnered significant attention for the low carbon transition of the petroleum industry. How to overcome the hardships from severe emulsion and interaction with soil minerals in emulsion–soil (OS) is a significant challenge with the prospective opportunities of solar energy substitution. This paper proposed the solar-driven photothermal conversion technology for efficient dehydration of OS and purification of oily water using a multifunctional material. A biomass-based carbon aerogel (BCA-600) with a porous three-dimensional (3D) structure and photothermal conversion characteristics was synthesized. Interestingly, this carbon aerogel possessed adjustable surface wettability, enabling it to adsorb high viscosity crude oil on the water surface (4.28 $g \cdot g^{-1}$) and achieve demulsification–separation in water-in-oil emulsions (97.28%) with the assistance of solar irradiation. Accordingly, the synergistic action of solar heating and separation–adsorption of emulsion by BCA-600 contributed to the efficient photothermal dehydration for both OS and emulsion. The highest dehydration efficiency for OS reached 90.68% with the OS/BCA-600 mass ratio of 10:2. Moreover, BCA-600 could remain in the dehydrated OS without separation to participate in the following pyrolysis with enhanced effects by confined-catalytic cracking, achieving a "one stone, two birds" effect. Overall, the solar photothermal approach exhibits significant potential for treating oily pollutants, reducing carbon emissions by more than 100 times compared to traditional thermal methods. This could be a strong push for the low carbon transition of the petroleum industry.

1. Introduction

The oil industry produces multiple pollution problems during extraction, transportation, and storage, such as oily wastewater and oily sludge (OS) [1–3]. Due to their high adsorption capacity, porous materials can adsorb and recover crude oil pollutants. However, because crude oil contains high levels of heavy components and exhibits high viscosity, its diffusion rate in porous materials is low, resulting in poor adsorption effect. Notably, the viscosity of crude oil decreases with an increase in temperature [4]. Ge et al. [5] proposed a graphene-wrapped sponge to adsorb crude oil from wastewater using joule heating, but it required a large amount of electricity. With the assistance of renewable solar energy, porous materials with photothermal conversion abilities should have a high potential for recovering spilled high-viscosity oil under solar irradiation. Kuang et al. [6] prepared a solar-heated carbon absorber with aligned channels and low curvature using natural wood for rapid adsorption of crude oil. Ding et al. [7] reported a biomass-based compressible aerogel to treat oily

* Corresponding authors.
E-mail addresses: chen@tju.edu.cn (G. Chen), houla@cae.cn (L. Hou).

https://doi.org/10.1016/j.eng.2025.01.008

wastewater, with the oil–water interface temperature exceeding 60 °C under sunlight irradiation. Wu et al. [8] designed a dual-function graphene device capable of simultaneously solar-powered steam generation and continuous oil recovery from oil-contaminated seawater. Due to their special pore size, pore structure, and surface wetting properties, some of these porous materials also effectively demulsify and separate oil–water emulsions. However, the application of photothermal porous materials in emulsion–soil (OS) treatment remains unexplored. OS mainly consists of petroleum hydrocarbons, water, and solid residue. Currently, pyrolysis can recover petroleum hydrocarbons through anaerobic heating and produce harmless residue with low oil content. However, most OS contains high water content and exhibits serious oil–water emulsification, posing significant challenges for dehydration before treatment and increasing energy consumption for pyrolysis due to water evaporation. Thermal dehydration is widely applied for OS and other waste with high water content but also requires additional energy input.

Solar energy is an inexhaustible source of clean energy that can be converted into heat energy by various photothermal conversion materials, such as metal nanoparticles [9], semiconductors [10,11], and carbon-based materials [12,13], which have been widely used in clean water evaporation devices. Numerous studies have demonstrated the potential of solar energy in the field of water evaporation. Peng et al. [14] modified wood with simple tannic acid and Fe^{3+} to impart photothermal conversion ability, achieving an evaporation rate of 1.85 $kg{\cdot}m^{-2}{\cdot}h^{-1}$ under 1.0 sun (100 $mW{\cdot}cm^{-1}$). Lee et al. [15] proposed a novel superhydrophilic thermal insulation macroporous film composed of carbonized sucrose and polydimethylsiloxane as an efficient solar evaporator, achieving an evaporation rate of 2.05 $kg{\cdot}m^{-2}{\cdot}h^{-1}$ under 1.0 sun. However, these studies are based on the theory of interfacial evaporation, making it challenging to use the interfacial evaporator to vaporize the water in the OS due to its high viscosity and high emulsification. Before the theory of interfacial evaporation was proposed, the volumetric evaporation strategy was used to disperse nanoscale photothermal conversion materials in water and heat the water body by *in-situ* light absorption [16,17]. Inspired by these approaches, we are interested in exploring the use of photothermal conversion for OS dehydration. With the assistance of photothermal materials, OS can heat up more rapidly under sunlight, thus accelerating water evaporation. However, due to the highly emulsified oil–water system in OS, the heat generated by the photothermal conversion material is absorbed by water and must overcome the coating film created by the heavy components of crude oil or surfactants. Therefore, the photothermal conversion materials that can promote the separation of the oil–water emulsion during the evaporation process have the potential to improve OS evaporation efficiency. Besides, the effect of oil and soil co-existence on solar photothermal evaporation remains unclear.

Compared to expensive carbon materials such as carbon nanotubes or graphene, biomass carbon-based materials are renewable, low cost, and easily degradable. Cellulose, an extract of biomass, is an ideal substrate for the preparation of three-dimensional (3D) materials. Many cellulose-based aerogels have been widely studied in the field of oil pollution treatment [18,19]. The porous aerogel prepared by combining cellulose with other biomass can effectively separate the oil–water emulsion [20]. Moreover, cellulose aerogel can be transformed into carbon aerogel by increasing the degree of graphitization and order through high temperature carbonization, thereby converting solar energy into heat energy through π electron transition and relaxation process [21]. Under the trend of clothing product innovation caused by social development and the improvement of human living standards, a large number of waste cotton textiles are accumulating. Cotton is a typical natural material, its main component is cellulose, so it is a promising material for the preparation of cellulosic carbon aerogel. For this purpose, we used common biomass materials, such as carboxymethyl cellulose (CMC) and cotton, to obtain a 3D porous skeleton through freeze-drying technology and achieve photothermal conversion performance through pyrolysis carbonization. The preparation process of the carbon aerogel material is simple and can meet the requirements of multiple types of oily pollutants with the assistance of solar energy, including the adsorption of leaked oil, treatment of oil–water emulsion, and natural dehydration of OS. This work provides new insights for low carbon transition during clean disposal of oily pollutants with prospective opportunities to involve renewable energy in the fields of OS and oily water.

2. Experimental section

2.1. Materials

CMC, methyltrimethoxysilane (MTMS), dichloromethane (DCM), hexane, and rhodamine B were obtained from Aladdin (China). Cotton and lubricating oil were bought from local supermarket, China. Crude oil and diesel oil were obtained from Daqing, China. Saline-alkali soil was acquired in Tianjin, China. $Cr(NO_3)_3$, $Cd(NO_3)_2$, $ZnCl_2$, $PbCl_2$, and $Cu(NO_3)_2$ were bought from Macklin (China).

2.2. Preparation of biomass-based carbon aerogel

Firstly, 3.0 g CMC was dissolved in 100 mL deionized water with addition of 0.4 g absorbent cotton after grinding for gelation. The resulting hydrogel was frozen at −80 °C for 6 h and placed in a vacuum freeze dryer for 48 h to completely remove the liquid phase and obtain the biomass-based aerogel (BA). Subsequently, BA was pyrolyzed at 300, 400, 500, and 600 °C for 1 h with a rate of 10 $°C{\cdot}min^{-1}$ under nitrogen atmosphere. After complete carbonization, the biomass-based carbon aerogel (BCA) was collected and named as BCA-*y*, where *y* is the carbonization temperature. In order to further enhance the oil–water selective wettability of BCA-*y*, hydrophobic treatment of BCA-*y* was performed by a simple silanization with assistance of MTMS. In simple terms, BCA-*y* was put together with two vials containing 2 mL of MTMS and 2 mL of deionized water in a sealed environment and heated at 80 °C for 3 h to obtain silane-modified BCA-*y*, such as SBCA-*y*.

2.3. Adsorption of organic solvent under solar heating conditions

Oil adsorption capacity is the critical factor for application. Xenon light source (CEL X250; power 250 W, spectral range 200–2500 nm) was used to provide the simulated sunlight (100 $mW{\cdot}cm^{-2}$, i.e., 1.0 sun) for the adsorption properties of SBCA-600. Diesel oil, crude oil, lubricating oil, DCM, and hexane were selected as organic solvents for adsorption. The sample was placed on the surface of organic solvents gently for 5 min. The mass difference after reaching saturation was calculated to evaluate the adsorption capacity. The absorption capacities (A) were evaluated with the equation:

$$A = (m_w - m_0)/m_0 \quad (1)$$

where m_w and m_0 are the weight of SBCA-600 before and after the absorption, respectively.

2.4. Separation efficiency test of SBCA-600 for various organic solvents and water

Add 36 mL deionized water and 4 mL organic solvent into the beaker, and mark the mass of the added organic solvent as m_1. According to the corresponding adsorption capacity of organic

solvent, a slightly excessive mass of SBCA-600 was added, and the mass of added SBCA-600 was marked as m_2. After 10 min of adsorption (xenon lamp was used to simulate sunlight when absorbing crude oil), take out SBCA-600 and record the mass at this time as m_3. The separation efficiency (S) of SBCA-600 for organic solvent was evaluated with the equation:

$$S = (m_3 - m_2)/m_1 \quad (2)$$

2.5. Preparation of OS

Crude oil and distilled water were mixed with pretreatment at 80 °C for viscosity reduction, and then stirred for 10 min on a homogenizer (FJ-200, Shanghai Huanalysis Industrial Co., Ltd., China) at 11 000 r·min^{-1}. The process was repeated twice to get a stable oil–water emulsion. The prepared emulsion remained stable at room temperature for several days without significant phase separation. Subsequently, saline-alkali soil was mixed with the prepared oil–water emulsion and stirred to simulate OS.

2.6. OS dehydration experiment

Firstly, 10.0 g OS was mixed with different amount of BCA-600 powder. Then put it on the surface of a petri dish which the drying dehydration experiment was carried out with the irradiation of simulated sunlight (1.0 sun). A xenon lamp was equipped to simulate the sunlight with adjustment of the optical power density. Specifically, the evaporation area was fixed at 50.24 cm^2 with evenly dispersion of the mixture of OS and BCA-600. The petri dish was placed on an electronic balance to record the mass change in real time, which can reflect the water evaporation rate. A thermal imaging camera (DT-9897, Shenzhen Huashengchang Technology Industrial Co., Ltd., China) was used to capture the thermal images of OS surface and reveal the photothermal performance with the temperature variation.

2.7. Characterization

The nitrogen sorption–desorption isotherm was performed on a specific surface area analyzer (BELSORP-max, Microtrac, Japan) and calculated according to Brunauer–Emmett–Teller (BET) method. The morphologies of samples were analyzed by scanning electron microscope (SEM; Quanta FEG 250, FEI, USA). The surface element composition of samples was analyzed by X-ray photoelectron spectroscopy (XPS; Escalab 250Xi, Thermo Fisher Scientific, USA). The spectra were determined using a photoelectron spectrometer with a standard Al Kα source (1486.6 eV), power 150 W, X-ray beam spot 500 μm and a pass energy of 30 eV was used in this situation. The surface functional group structure was analyzed by Fourier transform infrared (FTIR; NicoletTM iS50 FTIR, Thermo Fisher Scientific) spectrum. Thermal degradation behaviors were measured by an online thermogravimetry analyzer equipped with mass spectrometer (STA 449F3 Jupiter thermogravimetry analyzer, Netzsch, Germany).

3. Results and discussion

3.1. Physical and chemical properties of BCA-y

The preparation procedure of BCA-*y* is illustrated in Fig. 1(a). As the morphologies depicted in Fig. 1(b), BCA-*y* features a hybrid channel structure composed of amorphous and filamentous fiber carbon structures. The oxygen-containing groups rich in cotton fiber can crosslink with CMC well, and form a porous interconnected network structure as a supporting skeleton. CMC coated on the cotton fiber skeleton is freeze-dried to form random micrometer pores, and then the amorphous carbon obtained by pyrolysis jointly forms the main structure of BCA-*y*. Clearly, more submicron pores could be observed from SEM images for BCA-600. Besides, the pore size distribution curves also validated that BCA-600 possessed much more pores with lower pore width. With an increase in pyrolysis temperature, further pyrolysis of biochar at high temperatures contributed to the appearance of submicron pores on the skeleton of BCA-600 [22–24]. Fig. 1(c) presents the N_2 adsorption–desorption curve, indicating that all carbon aerogels were type II isotherms (classified by International Union of Pure and Applied Chemistry (IUPAC)). At low relative pressure (< 0.1), the adsorption capacity rose rapidly, and the curve was convex, proving that these materials were macroporous materials. With increasing pyrolysis temperature, BCA-*y* demonstrated higher adsorption–adsorbent interaction, attributable to the activation of the material at high temperatures [21]. Fig. 1(d) shows the pore size distribution of BCA-*y*. It can be evident that most of the materials with the largest pore volume had pore sizes less than 100 Å. These micropores likely resulted from the decomposition of biomass macromolecules. The pore volume in the range of 100 to 1000 Å decreases with increasing pyrolysis temperature, which can be attributed to skeleton collapse due to the higher pyrolysis temperatures [25]. In general, BCA-*y* shows the structural characteristics of the coexistence of micropores and macromicron pores. The large pores at micron level are conducive to providing sufficient space for the adsorption of organic solvents, while the small pores are conducive to the separation of oil–water emulsions [26–28].

3D materials with selective oil–water wettability and porous structure have been extensively studied for oil–water separation [29–31]. Materials with photothermal conversion capabilities can more effectively manage the separation of high-viscosity crude oil and water. The carbonization process contributes to pore formation, and removal of hydrophilic functional groups, and enhances photothermal conversion through the generation of conjugated π bonds. The oil–water selective wettability of BCA-*y* is illustrated in Fig. 2(a). Clearly, BA without pyrolysis treatment had a water contact angle of 0°, indicating super hydrophily. Pyrolysis immediately increased the water contact angle to 101.7° and exhibited slight variation with the elevation of pyrolysis temperature between 300 and 600 °C. The lower water contact angle indicated that BCA-*y* had an average ability to selectively separate oil from water. In order to obtain materials with selective oil–water separation ability for layered oil–water separation, we considered enhancing the hydrophobic ability of BCA-*y* by surface modification, which can be obtained by silane hydrolysis of MTMS. Dramatically, MTMS modification increased the water contact angle to 106.0° for SBCA without pyrolysis, indicating initial hydrophobicity. Further carbonization elevated the water contact angle from 130.9° of SBCA300 to 142.4° of SBCA-600, much higher than without MTMS modification. To some extent, MTMS can replace carbonization when the sole target is hydrophobic modification. Besides, SBCA-600 exhibited excellent lipophilicity that could rapidly adsorb oil droplets. The surface functional groups of BCA-*y* are reflected in FTIR spectra in Fig. 2(b), which mainly include aromatic O–H (3430 cm^{-1}), C–H (868 cm^{-1}), C=C (1585 cm^{-1}), C=O (1640 cm^{-1}), and C–O (1011cm^{-1}) [20,21]. These oxygen-containing functional groups were very weak in these BCA samples and almost disappeared for BCA-600, explaining the hydrophobicity after carbonization. Fig. 2(c) gives full XPS spectra for BCA-*y*, with four samples each having three dominant peaks at 532.1, 530.5, and 283.1eV, attributed to sodium Auger peak (Na KLL), O 1s, and C 1s, respectively. The Na element came from CMC. The miscellaneous peaks below 200 eV should originate from the impurities in cotton fibers with

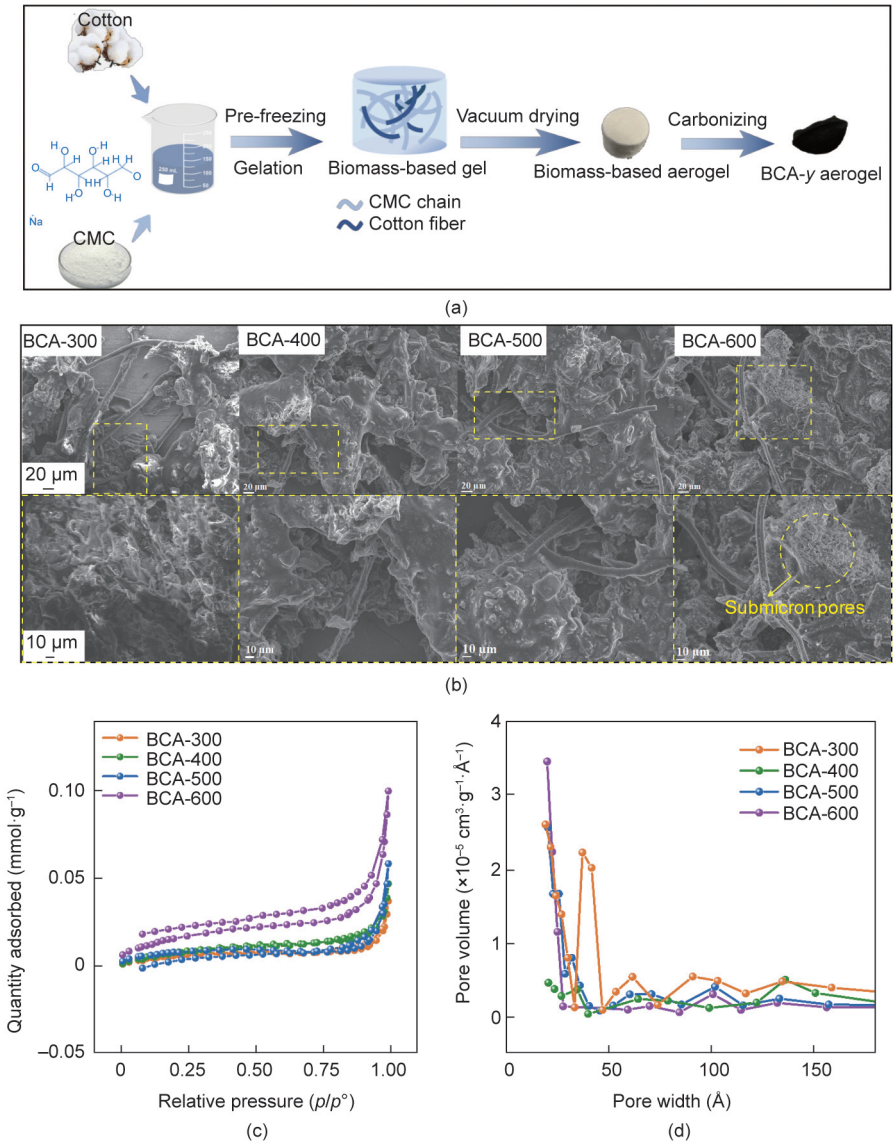

Fig. 1. (a) Schematic diagram of preparation process of BCA aerogel; (b) SEM images; (c) nitrogen adsorption–desorption isotherms (p: partial pressure of nitrogen, p^o: saturated vapor pressure of nitrogen); and (d) pore size distribution of BCA-y.

negligible content. The C 1s high-resolution XPS spectrum of BCA-y showed the presence of C–C, C–O, and C=O (Fig. S1 in Appendix A). With the increase in pyrolysis temperature, the percentage content of C–O decreased from 36.85% for BCA-300 to 21.28% for BCA-600, and the content of C=O decreased from 33.43% to 3.92%. The decrease in oxygen-containing functional groups led to the hydrophobicity of BCA-y, as confirmed by the conclusion of FTIR.

The photothermal conversion capacity is another critical factor affecting the separation effect on high-viscosity crude oil. Fig. 2(d) shows the absorption intensity of BCA-y on the solar spectrum. Clearly, the absorption energy of BCA-y on the solar spectrum became stronger continually with the elevation of carbonization temperature, especially in the near-infrared region (780–2500 nm). Subsequently, the photothermal temperature rise curves of BCA-y under simulated illumination (1.0 sun) are presented Fig. 2(e). BCA-600 rose from room temperature to 79.8 °C within 180 s, while BCA300 only reached 64.7 °C after 180 s, consistent with the absorption intensity of the solar spectrum. Fig. S2 in Appendix A shows the temperature–time change curve of BCA-600 under light with different CMC/cotton ratios. It can be seen that when the cotton content gradually increased, the surface equilibrium temperature of BCA-600 increased, and this trend was most obvious when the cotton content was less than 0.4 g. When the cotton content continued to increase to 0.6 and 0.8 g, the surface temperature increase effect was not obvious. This may be due to the fact that increasing the cotton content forms more graphitized structures conducive to photothermal conversion at high temperatures [32,33]. However continuing to increase the amount of cotton to increase the surface equilibrium temperature of BCA-600 also increased the heat radiation loss to the environment. Considering the photothermal conversion effect and economic cost, the CMC/cotton ratio of 3.0:0.4 (wight (w)/w) is more appropriate. Unless otherwise specified, the CMC/cotton ratio for all BCA-600 in this article is 3.0:0.4 (w/w). Fig. 2(f) presents the heating capacity of BCA-600 under different light power densities: 1.0, 1.5, and 2.0 sun. As expected, the equilibrium temperature of BCA-600 increased significantly with the increase in light power density. After 180 seconds, the equilibrium temperature reached 79.8, 98.5, and 117.7 °C respectively. Besides, the equilibrium temperature was reached within a shorter time under stronger light intensity. Fig. 2(g) displays the good cyclic stability of BCA-600, showing

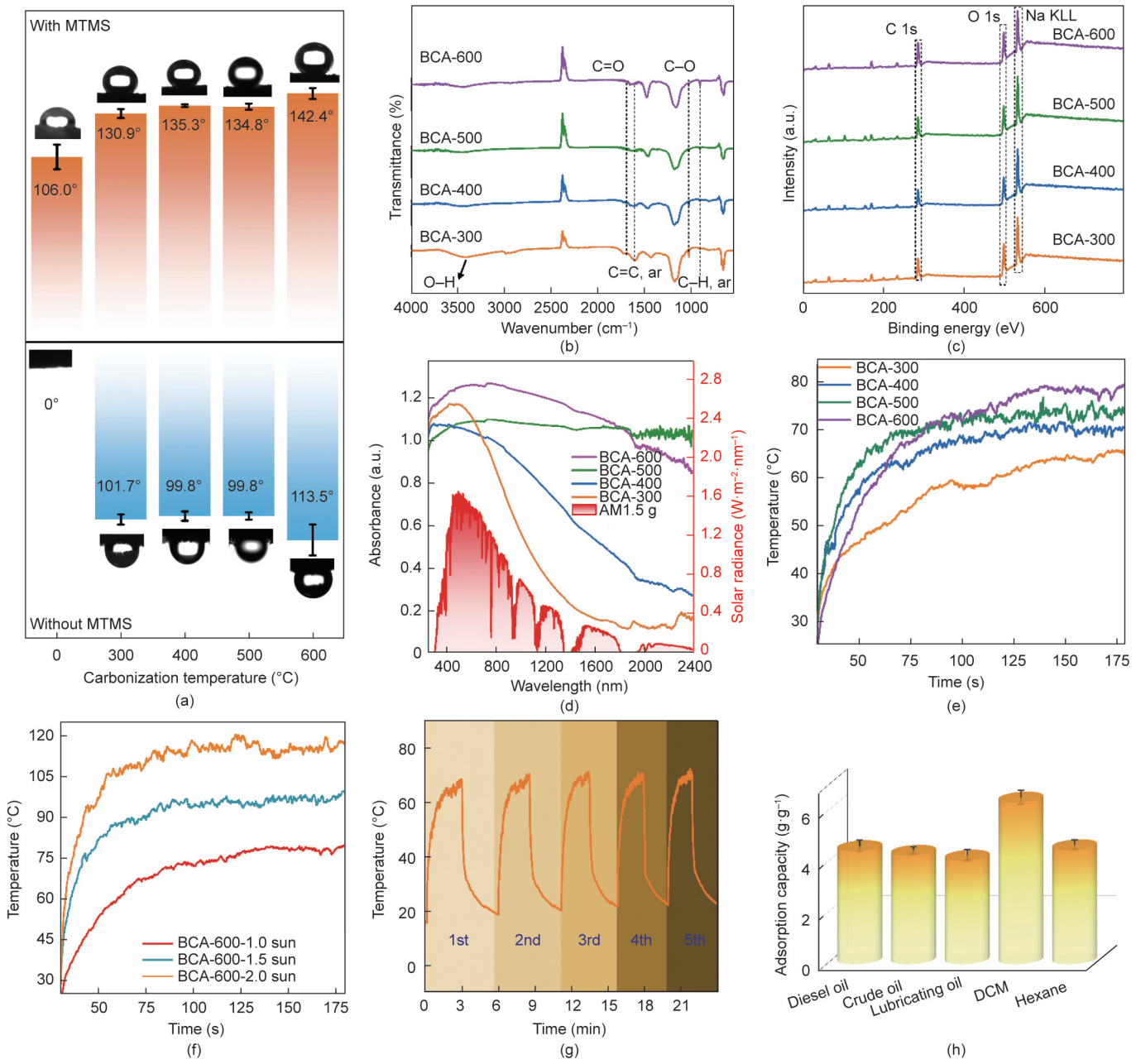

Fig. 2. (a) Water contact angle diagram, (b) FTIR spectra (ar: aromatic); (c) full XPS spectra, Na KLL: sodium auger peak; (d) solar absorption curves from 250 to 2500 nm (AM 1.5 g: standard spectrum of the Earth's surface); (e) temperature rising under 1.0 sun; (f) temperature rising of BCA-600 under different light power densities; (g) cyclic temperature rising of BCA-600 under 1.0 sun; and (h) adsorption capacity of organic solvents over SBCA-600 under 1.0 sun.

that the heating rate and equilibrium temperature of BCA-600 did not change significantly after five cyclic light tests. Therefore, BCA-600 possessed a good photothermal conversion efficiency and adjusted surface wettability for varied applied scenarios.

3.2. Oil adsorption and oil–water separation

Materials with excellent hydrophobicity and lipophilicity, such as SBCA-600, can selectively adsorb oil in oil–water mixture, making them a viable option for oil–water separation to some extent. Firstly, to evaluate the oil adsorption capacity, SBCA-600 was selected to directly adsorb various organic solvents in the absence of water under 1.0 sun. As presented in Fig. 2(h), SBCA-600 adsorbed about 4 to 6 times its own weight in organic solvents, and the adsorption capacity for high-viscosity crude oil reached 4.28 $g \cdot g^{-1}$. It can be speculated that its adsorption capacity would further increase under solar irradiation. Next, to assess the selective adsorption property in an oil–water mixture, SBCA-600 was placed on the surface of a stratified oil–water mixture with a water content of 90.0%, as presented in Fig. 3(a-i). To ensure separation efficiency, the dosage of SBCA-600 used was slightly more than the theoretical value needed for the saturated adsorption of the crude oil obtained from Fig. 2(h). The crude oil was almost fully adsorbed by SBCA-600 under 1.0 sun irradiation within 10 min, while SBCA-600 still floated on the water surface due to its excellent oil–water selective wettability (Fig. 3(a-ii)). A video of the SBCA-600 adsorbing crude oil under light is provided in Video S1 in Appendix A. The infrared image depicted in Fig. 3(a-iii) demonstrates that the surface of SBCA-600 reaches 54.1 °C, which is lower than the 79.8 °C achieved without the participation of oil. The

viscosity reduction and adsorption of crude oil were endothermic processes, directly contributing to the decline of surface temperature. Additionally, the partial covering and filling of oil molecules on the surface and in the internal pore channels inhibited photothermal conversion efficiency. The separation efficiency of SBCA-600 for the mixture of organic solvents and water is calculated and presented in Fig. 3(b), which all reached 96.88%–99.87%, proving the applicability of SBCA-600 for separation of organic solvents from oily wastewater.

Oily wastewater produced by the oil industry generally exists as a water-in-oil emulsion, which is more challenging to separate compared to the aforementioned stratified oil–water mixture. The water-in-oil emulsion contains many tiny water droplets, which are difficult to aggregate and separate spontaneously due to the action of surfactants or heavy components of crude oil. BCA-600 did not have a water contact angle of more than 120° in the air, which was not favorable for effectively separating layered oil and water due to a worse separation effect. Therefore, in the specifically target oil–water separation scenario, simple hydrolysis modification of silane was conducted to improve its oil–water selective adsorption capacity and improve the oil–water separation effect. However, demulsification was the critical step for the separation of water-in-oil emulsions, which tended to occur primarily inside the pores of the material without particularly significant changes in surface wettability [34]. Accordingly, considering the cost and process, MTMS modification was not further used in subsequent experiments in terms of emulsion treatment. BCA-600 with a relatively poorer hydrophobicity, might be more effective in this context. Furthermore, BCA-600 has the appropriate pore size and zigzag internal structure, which are favorable for the separation of water-in-oil emulsion. As shown in Fig. 3(c), BCA-600 was placed on the surface of an oil-in-water emulsion and connected to a peristaltic pump. The peristaltic pump drove the emulsion to flow through the inside of BCA-600, and the separated oil was collected at the pump's exit. The moisture content of the emulsion before and after separation was determined by Karl Fischer's water analyzer. Separation tests were conducted for hexane–water emulsion and diesel–water emulsion. Fig. 3(d) shows that the separation efficiency of hexane–water emulsion and diesel-water emulsion reaches 97.28% and 88.81%, respectively. Fig. 3(e) presents digital and electron microscope images before and after the separation of the two emulsions. Clearly, there was no significant free water after the separation for hexane–water emulsion, while a small amount of free water droplets was observed for diesel–water emulsions, corresponding to their respective separation efficiencies. The difference in dynamic viscosity between hexane and diesel likely contributed to this phenomenon. To reveal the separation behavior of BCA-600 for water-in-oil emulsion, the hexane–water emulsion was further investigated as a representative. Additionally, suitable dyes, such as rhodamine B, were added to track the oil and water droplets during the separation process (Fig. S3 in Appendix A). The trace of specific element N from rhodamine B can be reflected from energy dispersive X-ray spectroscopy (EDXS; Fig. S3(a-iii)), which clearly showed that the bottom part of BCA-600 contained more N element than the top part after separation. Therefore, the separation mechanism of BCA-600 for water-in-oil emulsion is similar to that of some reported porous 3D materials [35,36]. The water droplets continuously collide and aggregate to form large droplets after the emulsions flow through BCA-600 due to the pore size screening mechanism. Besides, the oil film formed in the pores further promoted the aggregation of water droplets, ultimately achieving the separation of oil and water.

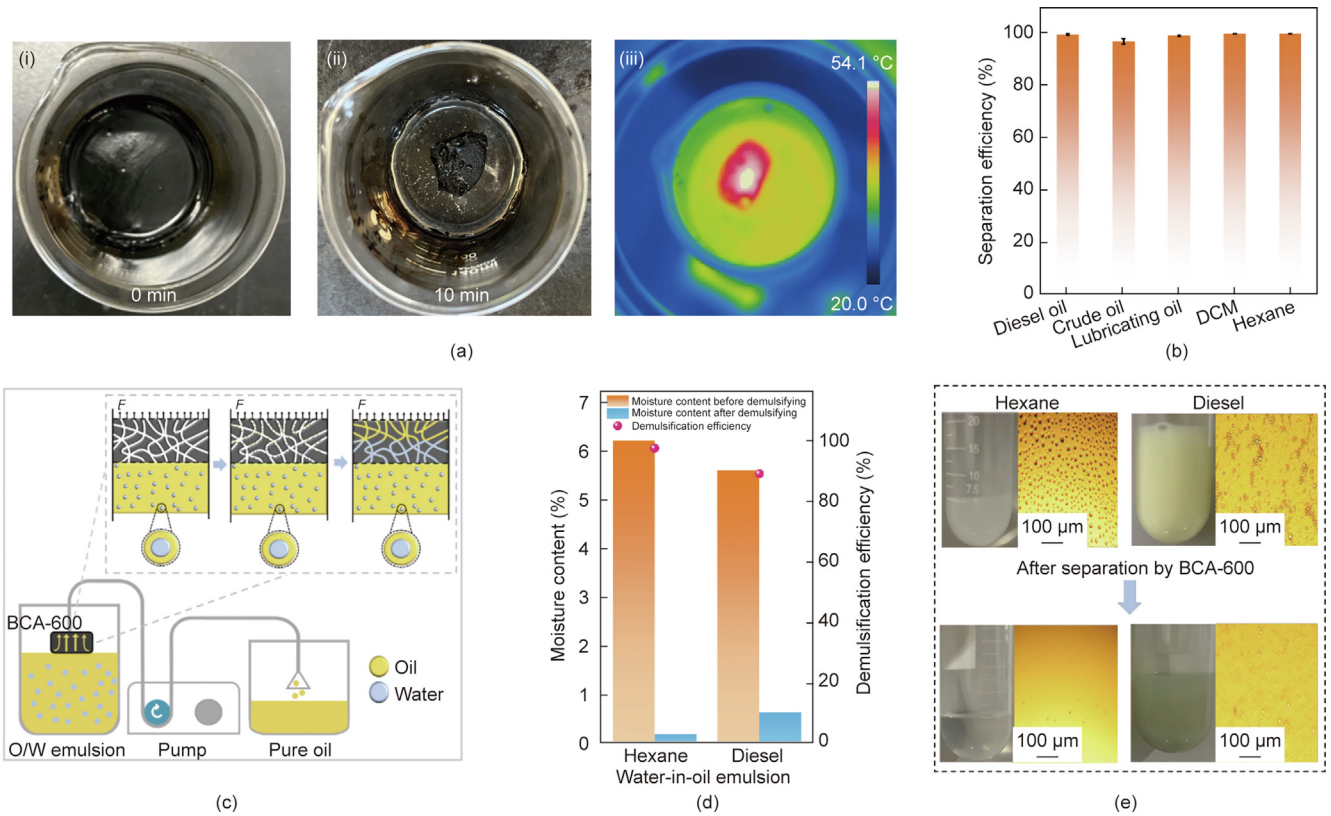

Fig. 3. (a) Diagram of SBCA-600 adsorbing crude oil on water surface under 1.0 sun at (a-i) 0 min and (a-ii) 10 min and (a-iii) its infrared image; (b) separation efficiency of SBCA-600 for various organic solvents and water; (c) schematic diagram of demulsification mechanism of BCA-600 (O: oil, W: water, *F*: driving force, from peristaltic pump); (d) moisture content and demulsification efficiency; and (e) photos and light microscopy of two emulsions before and after BCA-600 separation.

3.3. Promoting evaporation and dehydration

The photothermal conversion property of BCA-600 has the potential to promote evaporation and dehydration processes (Fig. 4). As mentioned above, OS is a type of solid waste containing a certain amount of water that needs to be removed before post-treatment. To evaluate the feasibility of solar-driven evaporation and dehydration of oily wastewater and wet soil, different amounts of BCA-600 were mixed with 10.0 g of water-in-oil emulsion to conduct water evaporation experiments using *in-situ* absorption of solar radiation energy. The dosage of BCA-600 was based on the saturated adsorption of crude oil. Under normal circumstances, crude oil is more likely to warm up than water due to its lower specific heat capacity. However, since the water droplets in the emulsion were coated with crude oil, water evaporation for water-in-oil emulsion becomes a tough problem. The relative content of oil and water in water-in-oil emulsion may impact evaporation. Figs. 4(a) and (b) present the mass change and its rate, calculated by differentiating of emulsion under 1.0 sun for 3 h with different oil/water mass ratios of 4:6, 5:5, 6:4, and 7:3. As expected, higher water content resulted in larger mass change and rate. The maximum weight loss reached 402.0 $g \cdot m^{-2}$ for the emulsion with an oil/water mass ratio of 4:6. The mass change rate rapidly reached the maximum value within 40–50 min and then declined slowly. Besides, the lower crude oil content led to an earlier peak in the maximum weight loss rate. Interestingly, the emulsions with higher oil/water mass ratios of 6:4 and 7:3 exhibited similar curves of mass change and its rate.

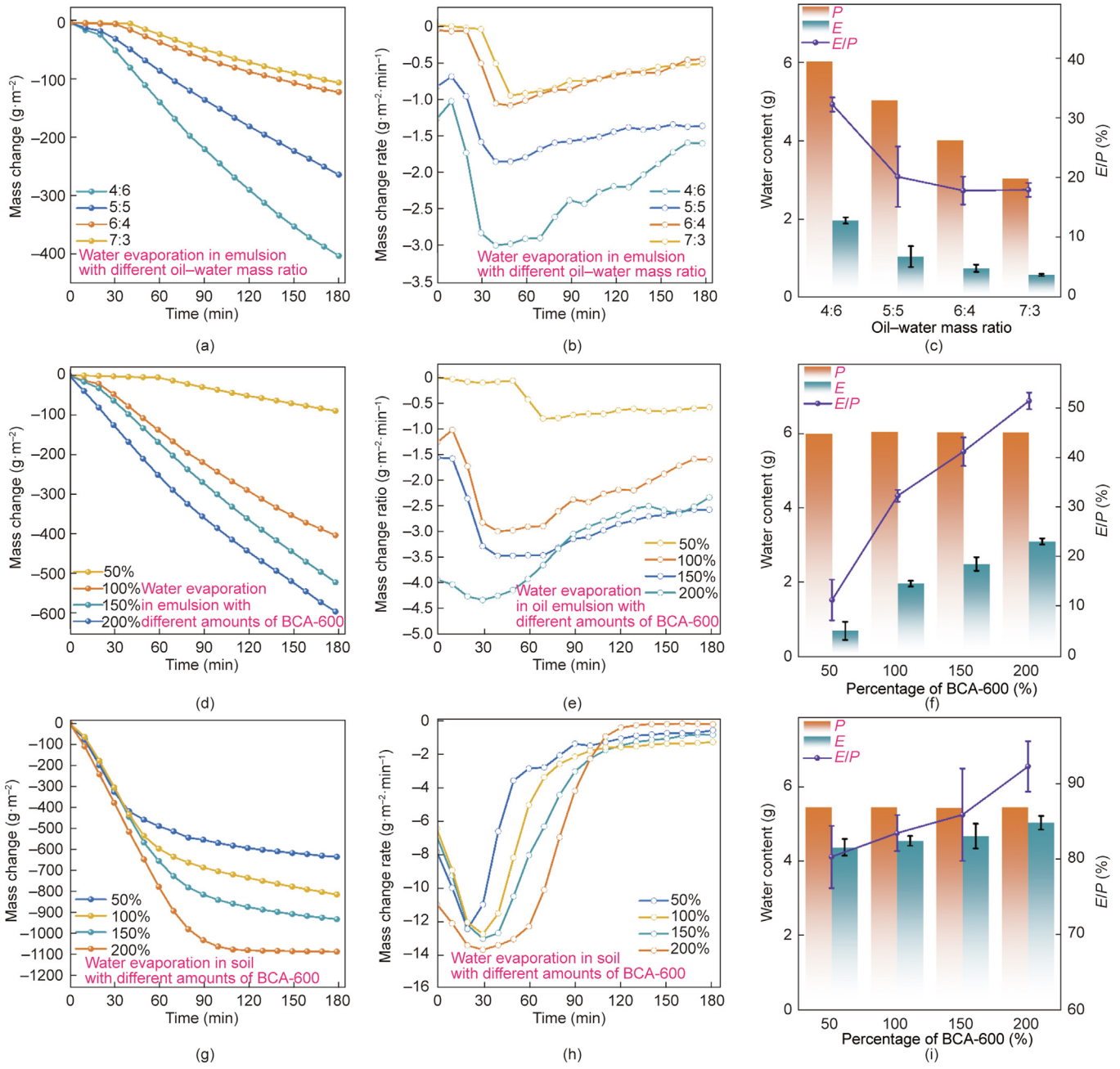

Fig. 4. (a–c) Evaporation of crude oil emulsion with a different oil–water ratio by 100% BCA-600; (d–f) evaporation of crude oil emulsion with the oil–water ratio of 6:4 by different amount of BCA-600; (g–i) evaporation of soil–water mixture with soil–water ratio of 6:5 by 100% BCA-600. (a, d, g) Mass change, (b, e, h) mass change rate, and (c, f, i) comparison between practical water content and evaporated mass loss with BCA-600. *P*: practical water content; *E*: evaporated mass loss.

Therefore, the high oil content caused more severe water-in-oil emulsion, making water evaporation more difficult. Fig. S4(a) in Appendix A depicts the temperature variation curves of the emulsion surface, which quickly rose to 35–45 °C within 40 min and maintained stable thereafter. The final temperature distribution is shown in the infrared images in Fig. S4(b). Lower water content attained higher temperatures, which also explains the lower temperature elevation in emulsion compared to the pristine BCA-600, as water evaporation absorbs a certain amount of heat. The practical water content (P) and evaporated mass loss (E) of these emulsions are shown in Fig. 4(c). Unfortunately, the actual weight loss was much lower than the practical water content, with the maximum ratio of E/P being 32.13%, indicating an undesirable dehydration effect.

To investigate the effect of the mixing amounts of BCA-600 on the evaporation of oil–water emulsions, 10.0 g of crude oil emulsions with an oil/water mass ratio of 6:4 was used with varied percentages of BCA-600 based on the saturated adsorption of crude oil. As presented in Figs. 4(d) and (e), more BCA-600 favored water evaporation, with the maximum mass change reaching 594.9 $g{\cdot}m^{-2}$ with the addition of 200% BCA-600. However, water evaporation was very slow when the BCA-600 was insufficient to completely adsorb the emulsion. Light irradiation on BCA-600 caused temperature rise, which further reduced viscosity. Consequently, the crude oil flowed and covered the surface of BCA-600, inhibiting the photothermal conversion effect. However, excessive BCA-600 could contain the emulsion inside its channel without overflow, thus alleviating the inhibition from the flowing emulsion (Fig. S5 in Appendix A). The weight loss rate curves also presented that excessive BCA-600 exhibited the highest rate initially, mainly due to the complete adsorption of emulsion inside its channels. This is also the reason why, in Figs. 4 (b) and (e), the evaporation weight loss rate in the early stage of the emulsion basically conforms to the trend of maintaining a stable first and then increasing. The idle material could promote the photothermal evaporation process. Besides, the idle channels of BCA-600 enhanced heat transfer efficiency. As presented in Fig. 4(f), the highest E/P value reached 51.22% for 200% BCA-600, while it was only 11.17% for 50% BCA-600.

Clearly, 51.22% is not a satisficed result for dehydration of emulsion. The oil phase component in the emulsion negatively impacts evaporation. These results illustrate that BCA-600 can promote evaporation and dehydration in an oil-in-water emulsion, but the emulsion also presents challenges. Subsequently, a soil–water mixture with a weight mass ratio of 6:5 was used to investigate the practical evaporation potential under sunlight with BCA-600. The amount of BCA-600 used was the same as in Fig. 4(d). Interestingly, the mass change was much faster in the soil–water system, almost reaching equilibrium within 90 min (Fig. 4(g)), while the emulsion system did not complete until 180 min. Besides, the insufficient addition of BCA-600 still attained a maximum weight loss of 80.37% (Fig. 4(i)), and the surface of the soil–water mixture hardened obviously after light exposure for 3 h (Fig. S6 in Appendix A). With the increase in BCA-600 addition, the maximum weight loss rate also increased (Fig. 4(h)). Additionally, the rate decreased much faster after reaching the maximum value for each soil–water subject compared to the emulsion. The equilibrium weight loss rate for the soil–water mixture with 200% BCA-600 was very close to zero, implying the free water is basically removed, but there is still a small amount of water that is difficult to remove, such as bound water. This was consistent with the E/P value of 93.40% presented in Fig. 4(i). It should be noted that 50% BCA-600 had the lowest ratio at 80.37%, but it was still much higher than the emulsion system in Fig. 4(d). In the oil–water emulsion system, there were two types of liquid: oil and water. Oil remained throughout the evaporation process, occupying the channels of BCA-600 and inhibiting heat transfer. Although BCA-600 exhibited demulsification effects that could release the water phase from the oil phase, water tended to sink due to density contrast or still physically mixed with oil in the same layer, further inhibiting water evaporation. Finally, the soil phase might play a role in promoting heat transfer during the evaporation process, allowing the heat generated by BCA-600 to transfer to the bottom faster, thereby accelerating the overall evaporation rate.

Based on the speculation, OS evaporation experiments were conducted to explore the effect of soil particles on the evaporation process by adding soil particles to a crude oil–water emulsion with a fixed oil–water mass ratio of 6:4, where 6:4:X represented the weight proportion of each phase (X is the mass of the solid phase). BCA-600 was also added according to the saturated adsorption of crude oil. As presented in Fig. 5(a), increasing the solid content contributed to a larger mass change in the first 60 min, but OS (6:4:20.0) quickly reached equilibrium without further increase. It should be noted that the higher content of solid particles caused lower water content in the entire OS system. Nevertheless, the mass change rate displayed in Fig. 5(b) illustrated that the presence of solid particles enhanced water evaporation, with the maximum value reaching 6.58 $g{\cdot}m^{-2}{\cdot}min^{-1}$ within 10 min for OS (6:4:20.0). After that, it quickly declined to approximately zero, implying ending of dehydration. Fig. 5(c) clearly depicts the promoting effect of solid particles on water evaporation, as the E/P value continuously increased with the content of solid particles. The E/P value for OS (6:4:20.0) had reached approximately 100%, implying almost complete dehydration. On one hand, higher content particles implied less water content, which reduced the evaporation energy consumption and contributed to a relatively higher surface temperature (Fig. S7 in Appendix A). On the other hand, the presence of solid particles should promote heat transfer due to their loose character and low specific heat capacity. Therefore, OS with higher solid content should exhibit better photothermal evaporation performance. Besides, complete dehydration is not the final target, which is meaningless if it requires too long-time an operation or too much input of materials. Reducing the water content with reasonable investment to alleviate the energy consumption for the post pyrolysis is the critical target for solar-driven dehydration of OS.

In the evaporation experiments of oil–water emulsion, the amount of BCA-600 was determined according to the theoretical saturated adsorption capacity of BCA-600 for crude oil. However, the difference in moisture content in the emulsion may affect the actual adsorption capacity of BCA-600. A higher amount of BCA-600 can significantly improve the dehydration efficiency of emulsion but will also increase the cost. Based on the promotion effect of solid particles in the OS system, it would be better to find a suitable mixture ratio of OS and BCA-600 that can attain acceptable dehydration efficiency while reducing the dosage of BCA-600 as much as possible. Subsequently, OS with a fixed oil/water/solid mass ratio of 6:4:5 (water content 26.7%) was selected with different BCA-600 mixing amounts to carry photothermal evaporation. As expected, the natural evaporation of pristine OS was very slow, while adding more BCA-600 accelerated mass change, with the highest rate reaching 4.58 $g{\cdot}m^{-2}{\cdot}min^{-1}$ (Figs. 5(d) and (e)). The pristine OS attained a mass change of 215.36 $g{\cdot}m^{-2}$ after 180 min, compared to only 119.43 $g{\cdot}m^{-2}$ for the emulsion (Fig. 4(a)), further validating the promotion effect of solid phase components in OS. When the mass ratio of OS to BCA-600 reached 10:2.0, the final mass change was 488.85 $g{\cdot}m^{-2}$, which was 2.27 times the original OS. The mass change rate curve of this sample was obviously different from others. Less BCA-600 caused free emulsion to float on the surface during the evaporation process, affecting the heat transfer effect. The photos before and after evaporation of OS with different BCA-600 mixing ratios in Fig. S8 in Appendix

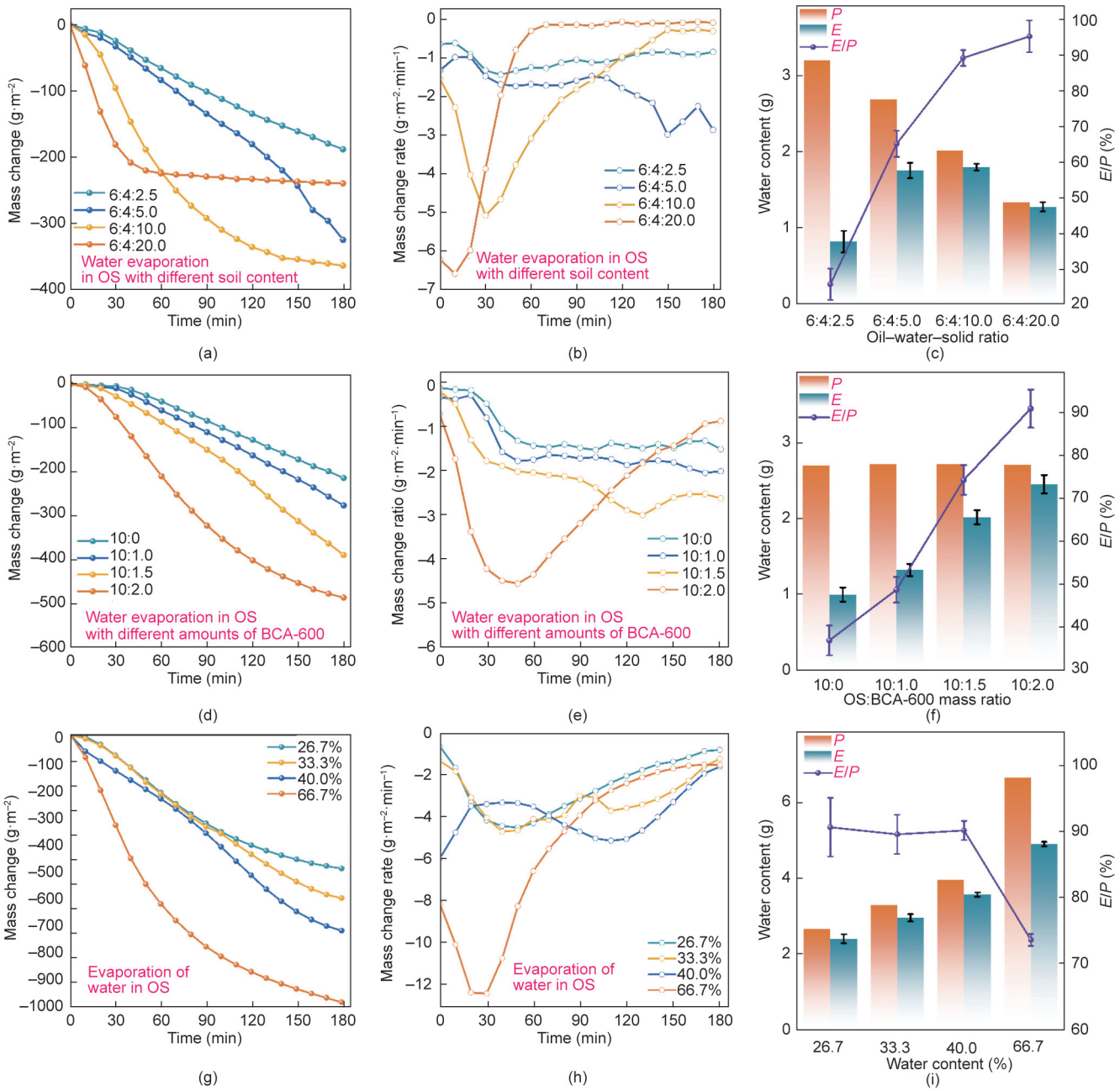

Fig. 5. (a–c) Evaporation of crude OS with different solid contents; (d–f) evaporation of OS with the oil–water–solid ratio of 6:4:5 by different amounts of BCA-600; (g–i) evaporation of OS with different water content. (a, d, g) Mass change, (b, e, h) mass change rate, and (c, f, i) comparison between practical water content and evaporated mass loss with BCA-600.

A present an obvious drying effect for the optimized sample, while there were still free emulsions for the other three experimental groups. Fig. 5(f) illustrates that the *E*/*P* value also increases with the elevation of BCA-600, and the dehydration rate can reach 90.68% under the OS to BCA-600 mass ratio of 10:2.0, which has exceeded the soil and water mixture (Fig. 4(i)). For the OS to BCA-600 mass ratio of 10:2.0, the percentage of BCA-600 based on saturated adsorption of crude oil was 74.90%, which was lower than 100% BCA-600.

To verify the applicability of BCA-600 for OS with different water content, a series of OS samples were prepared with varied oil–water ratios and mixed with BCA-600 according to the OS: BCA-600 mass ratio of 10:2.0. Fig. 5(g) clearly shows the mass change increases with elevation of water content at same evaporation time, while the OS sample with a water content of 66.7% climbed significantly compared to the other three samples. It should be emphasized that 66.7% water content represented the absence of an oil phase, such as, it was a soil–water mixture. Therefore, the presence of oil, especially emulsion, indeed inhibited water evaporation, and removal of the oil released the huge potential for water evaporation. Fig. 5(h) also displays that the maximum rate appeared slightly earlier for the soil–water mixture than other groups, which also reached the same level as Fig. 4(h), likely due to the absence of oil phase content leading to less free emulsion on surface evaporation. The evaporated mass loss increased slightly with the elevation of water content as depicted in Fig. 5(i). Interestingly, the *E*/*P* value maintained a relatively stable level for the first three OS samples, approximately 89.65% to 90.72%, while it declined to 73.27% for the soil–water mixture. Actually, 73.27% was lower than the lowest *E*/*P* value shown in

Fig. 4(i), which should be attributed to the lower water content in Fig. 4(i) which was only 45.4% and accordingly required less time to complete evaporation. An obvious drop in surface temperature observed from the infrared image (Fig. S9 in Appendix A) also reflected this phenomenon.

Clearly, BCA-600 had an excellent promotion effect on OS dehydration under sunlight, which should be attributed to its photothermal conversion and emulsion separation ability. BCA-600's macroporous and microporous structure could adsorb the emulsion, thus reducing the resistance to water evaporation. To illustrate that OS dehydration was not just influenced by solar heating, commercial carbon black (CB) with good photothermal conversion properties but no specific surface characteristics and lacking macropores was used for comparison with the same adding proportion, circa (ca.) 10:2.0 for OS and CB. As presented in Fig. S10 in Appendix A, the dehydration rate of OS/CB is far worse than that of OS/BCA-600. Therefore, the simple photothermal conversion effect may be insufficient, and the surface and pore structure are equally important for the separation synergy of oil–water emulsions.

Increasing the evaporation area can indeed improve the efficiency of evaporation, but it also leads to greater land occupation. Therefore, it is necessary to consider the utilized area comprehensively from the prospective of a practical photothermal dehydration process. With the same target amount of OS for treatment, maintaining the same evaporation area implies an increase in the accumulation thickness, which undoubtedly increases the difficulty of surface heat transfer and bottom water transmission upward. The suitable thickness of OS deposition determines the maximum single processing scale. Three OS samples with a fixed oil/water/solid mass ratio of 6:4:5, ca. 10.0, 20.0, and 30.0 g, were mixed with BCA-600 according to the OS/BCA-600 mass ratio of 10:2 and put into a container with a cross-sectional area of 5 cm × 5 cm. The accumulated thickness was 0.6, 1.2, and 1.7 cm. As expected, the mass change became slower with increasing thickness as presented in Fig. 6(a). Especially, when the thickness increased to 1.7 cm, the water evaporation became very slow (Fig. 6(b)), and the final evaporated mass loss was negligible (Fig. 6(c)). This can be seen from the side infrared thermal images of OS of three thickens 30 min before evaporation in Fig. 6(d). Besides, the mass change rate curves for all three groups followed the trend of increasing first and then maintaining stability (Fig. 6(b)), which were totally different from the above-mentioned results with an evaporation area of 50.24 cm^2. A small evaporation area caused a slow surface evaporation rate and accordingly prolonged the time to reach the maximum evaporation rate. The E/P value declined significantly with the increase in thickness. When the thickness was 1.7 cm, only 8.26% of the water was evaporated (Fig. 6(c)). Therefore, it would be better to carry out photothermal evaporation treatment of OS in batches with a lighter thickness to ensure efficient dehydration.

In summary, the solar evaporation and dewatering effect of photothermal conversion materials on OS is mainly restricted by many aspects. One is the characteristics and dosage of photothermal conversion materials. For porous photothermal materials with suitable surface wettability and pore structure, increasing the addition amount is an effective way to improve evaporation efficiency, and the specific addition amount should be determined according to the adsorption capacity of the material. The other one is the oil–water–solid three-phase relative content of OS. Simply speaking, the presence of the oil phase is not conducive to evaporation. Overcoming the oil-in-water emulsion barrier consumes a lot of energy and absorbs a lot of heat for water evaporation. Therefore, OS with high oil content will lead to a decrease in the evaporation effect, which needs to be avoided in practical applications. The presence of a solid phase facilitates evaporation, which is caused by the promotion of the relative heat transfer of solid, so different solid phase components and contents may theoretically have different effects on evaporation. The last one is the selection of evaporation area and thickness of OS. It is beneficial to increase the evaporation area and reduce the evaporation thickness, which accords with the influence factors of water evaporation under natural conditions. Therefore, in the face of actual application scenarios, it is necessary to choose the appropriate way and scheme according to the above aspects.

3.4. Water analysis from the evaporation of OS

During evaporation and dehydration of OS with the assistance of BCA-600, the temperature within the mixture can reach approximately 60–70 °C. At this temperature, a small amount of volatile organic compounds (VOCs) might be released [37]. Additionally, OS contains heavy metals, some of which may form water-soluble heavy metal salts that dissolve in the water phase. Whether these heavy metals volatilize with steam during evaporation is a critical factor for practical applications. To asses this, evaporated water was collected from the OS with a moisture content of 26.7% (oil–water–solid mass ratio of 6:4:5) and analyzed for its components. To simulate the heavy metals in OS, five heavy metal salts $Cr(NO_3)_3$, Cd $(NO_3)_2$, $ZnCl_2$, $PbCl_2$, and $Cu(NO_3)_2$ were added to the OS system. The OS samples were labeled as OS (1.0), OS (2.0), OS (3.0), and OS (4.0), corresponding to the respective concentrations of 1000, 2000, 3000, and 4000 $mg{\cdot}kg^{-1}$ for each heavy metal, respectively. As presented in Fig. 7(a), OS inevitably emits VOCs during evaporation. Fig. 7(b) illustrates the heavy metal content in the evaporated water from the above-mentioned OS samples. As the initial concentration of heavy metals increased, their content in the evaporated water also increased, particularly for Cr, Cd, and Cu. Zn and Pb had the highest concentration in the evaporated water due to higher volatility, which also caused fluctuations of experimental errors. According to the comprehensive sewage discharge standard of the People's Republic of China GB8978–1996, the contents of Cd and Pb in the evaporated water exceeded the permissible levels. Therefore, it is crucial to consider the filtering function of the evaporated materials to prevent the emission of pollutants from OS. The photothermal effect even accelerates the emission of these pollutants according to the basic physical principles. Effective filtering and containment strategies are necessary to mitigate the release of harmful substances during the photothermal dehydration process.

3.5. Co-pyrolysis behavior of BCA-600 and OS

After dehydration, OS requires further treatment to remove the oil phase through a pyrolysis process. Since BCA-600 was mixed with OS during the photothermal dehydration process and is difficult to separate, understanding their co-pyrolysis behavior is essential. BCA-600 is a carbonous material rich in oxygen-containing groups, such as –COOH, –OH, and so forth, which can effectively catalyze the pyrolysis reactions of oil molecules [38–40]. To investigate this, OS samples were prepared by mixing oil with soil (without water), maintaining an oil–water–soil mass ratio was 6:0:5. Various mass ratios of OS to BCA-600 were tested: approximately 10:3, 10:2, and 10:1, labeled as HA, FA, and OA, respectively. Fig. 8(a) presents the thermogravimetric (TG) curves of the three samples under an inert atmosphere, with the pristine OS and BCA-600 as benchmarks. The calculated TG curves (shown by the line) were derived from the mathematical addition of the two benchmark curves according to the proportions. Clearly, BCA-600 was very stable with negligible weight loss along the whole pyrolysis process. Under the same pyrolysis conditions, the observed weight losses of FA and OA were higher than the

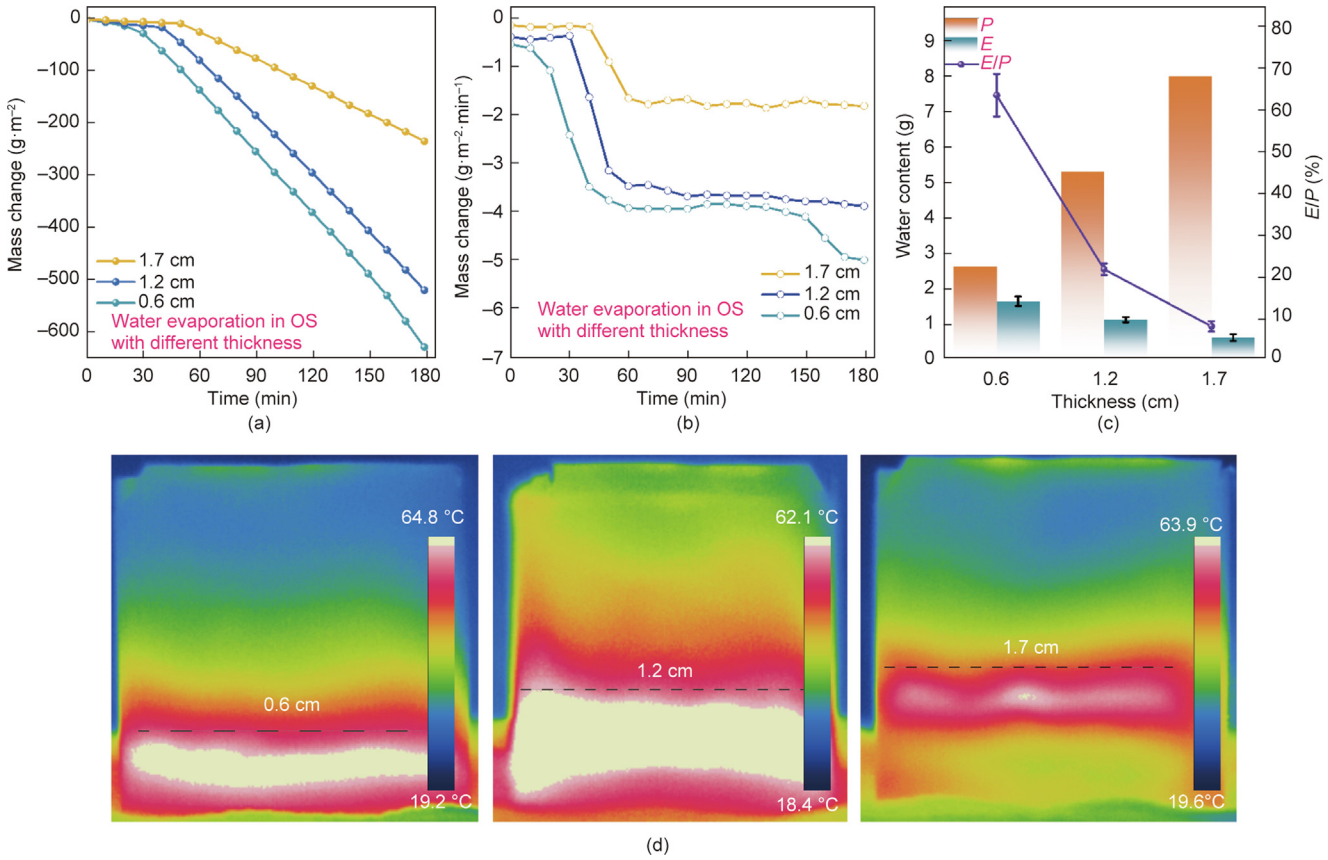

Fig. 6. Evaporation of OS mixed with BCA-600 under different thicknesses. (a) Mass change; (b) mass change rate; (c) comparison between practical water content and evaporated mass loss; and (d) infrared radiation images after 1.0 sum irradiation for 30 min.

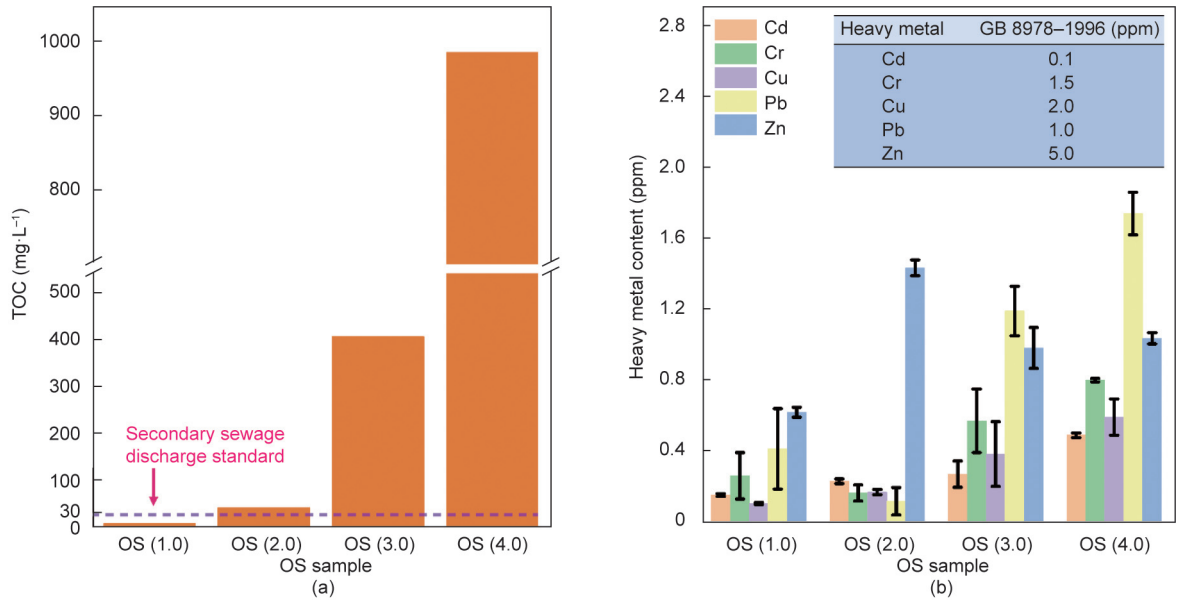

Fig. 7. (a) TOC and (b) heavy metal content of condensed water from evaporation of OS (ppm: parts per million).

calculated values, but HA was in contrast, implying that BCA-600 enhanced OS pyrolysis, but excessive addition caused an inhibition effect. Nevertheless, the inhibition effect was not presence before 480 °C. The derivative thermogravimetric DTG curves (Figs. 8(b-i)–(b-iii)) exhibited three characteristic regions by deconvolution through Gaussian functions. The first stage (S_I) mainly involved the removal of bound water and the volatilization of some light hydrocarbons, while the second (S_{II}) and the third stage (S_{III}) represented the volatilization of organic matter and the pyrolysis polymerization reaction, respectively [38]. In comparison, the absence of free water obviously weakened S_I, which was also similar for these three groups. However, S_{II} and S_{III} exhibited

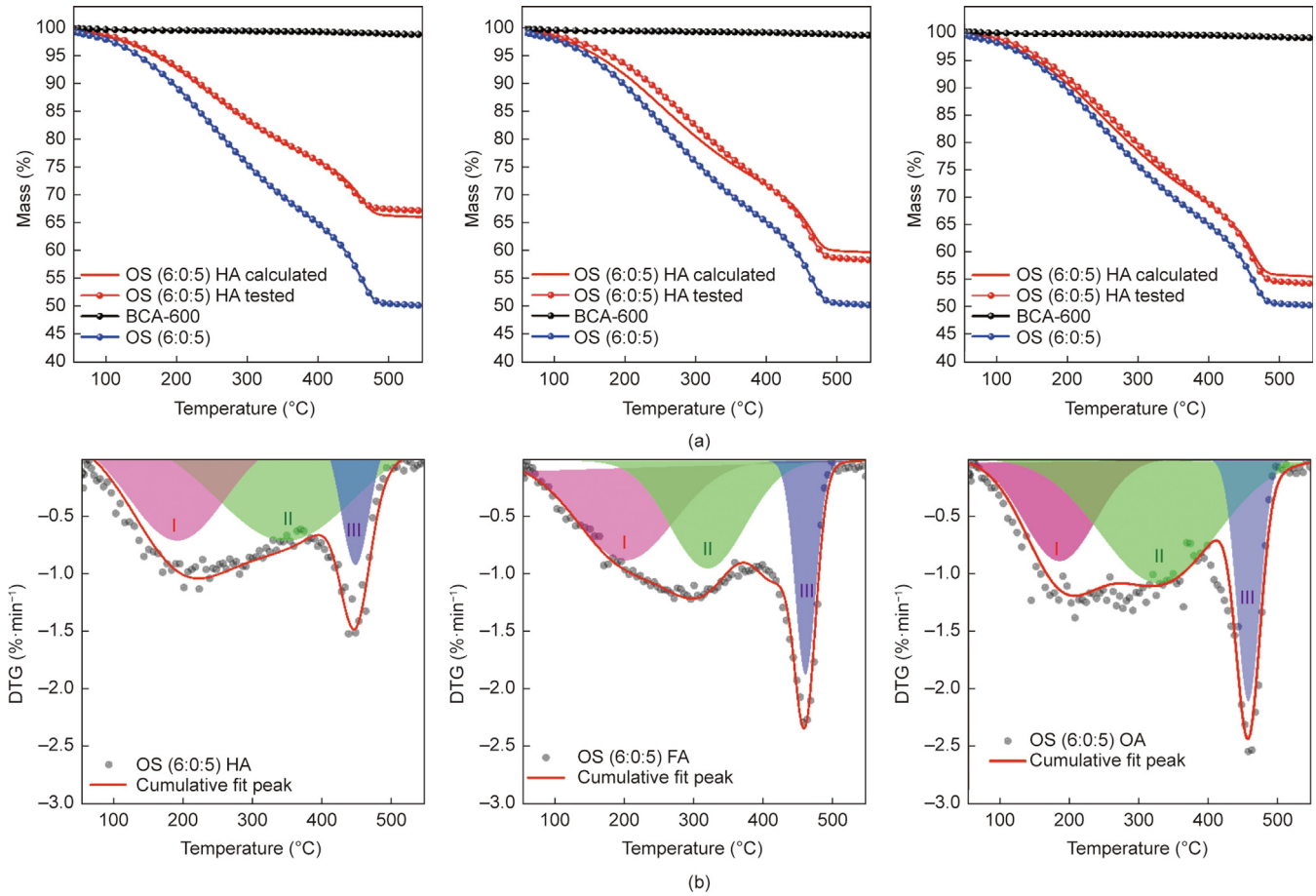

Fig. 8. (a) TG and (b) DTG curves of OS, BCA-600, and OS mixed with BCA-600 in different ratios, respectively.

differences that became stronger with the decline of the BCA-600 amount. Therefore, the presence of BCA-600 should enhance the desorption and decomposition of oil hydrocarbons, especially wean the polymerization reactions (S_{III}). Although HA exhibited a slight inhibition effect from the comparison between tested and calculated TG curves in the final stage, DTG curves also demonstrated that S_{III} was greatly weakened and that OS pyrolysis should be improved. Coats–Redfern method was used to compare the stage and the average activation energy and Avrami–Erofeev function was adopted to investigate the kinetic mechanism. As tabulated in Table 1, the activation energy in the S_{III} stage decreased from 103.42 kJ·mol^{-1} of alone pyrolysis (AP) of OS to 100.31, 93.35, and 83.30 kJ·mol^{-1} of OA, FA, and HA, respectively. Accordingly, the total average activation energy decreased from 48.59 to 40.64, 43.11, and 33.61 kJ·mol^{-1}, respectively. This meant that BCA-600 indeed played a positive role in reducing the activation energy of OS pyrolysis, which should mainly originate from polymerization. The porosity of BCA-600 allows it to adsorb oil hydrocarbons from mineral gaps into its carbon channels, facilitating the separation of oil and minerals. Previous literature has reported that parts of minerals aggravated polymerization [41,42]. Therefore, the separation of oil and minerals can alleviate the polymerization, which can contribute to the decline of activation energy. Besides, the abundant functional groups could interact with oil hydrocarbons, promoting cracking reactions. In conclusion, BCA-600 proves beneficial in enhancing the pyrolysis of OS after completing its role in the photothermal dehydration process, achieving dual functionality in environmental remediation processes.

3.6. Carbon reduction potential from solar photothermal dehydration of OS

Solar photothermal dehydration of OS aims to reduce traditional energy consumption and carbon emissions. A comparison between the carbon emissions of traditional thermal dehydration and solar photothermal dehydration is necessary. Figs. 9(a) and

Table 1
The activation energy (E_a) was obtained from the Coats–Redfern method.

Item	Stage	Temperature (°C)	E_a (kJ·mol^{-1})	R^2	α (%)	$\overline{E_a}$ (kJ·mol^{-1})
OS (6:0:5) AP	S_{II}	306.64–433.45	9.49	0.99	27.47	48.59
	S_{III}	433.45–500.00	103.42	0.96	19.59	
OS (6:0:5) HA	S_{II}	256.54–426.48	11.24	0.99	42.18	33.61
	S_{III}	426.48–500.00	83.30	0.98	18.98	
OS (6:0:5) FA	S_{II}	265.03–426.53	13.70	0.99	41.61	43.11
	S_{III}	426.53–500.00	93.35	0.95	24.36	
OS (6:0:5) OA	S_{II}	232.37–430.69	12.37	0.99	48.19	40.64
	S_{III}	430.69–500.00	100.31	0.96	22.83	

R^2: square of the correlation coefficient, α: mass conversion rate, $\overline{E_a}$: average E_a, which is the E_a of the whole process of hydrocarbon decomposition obtained by weighting E_a at each stage.

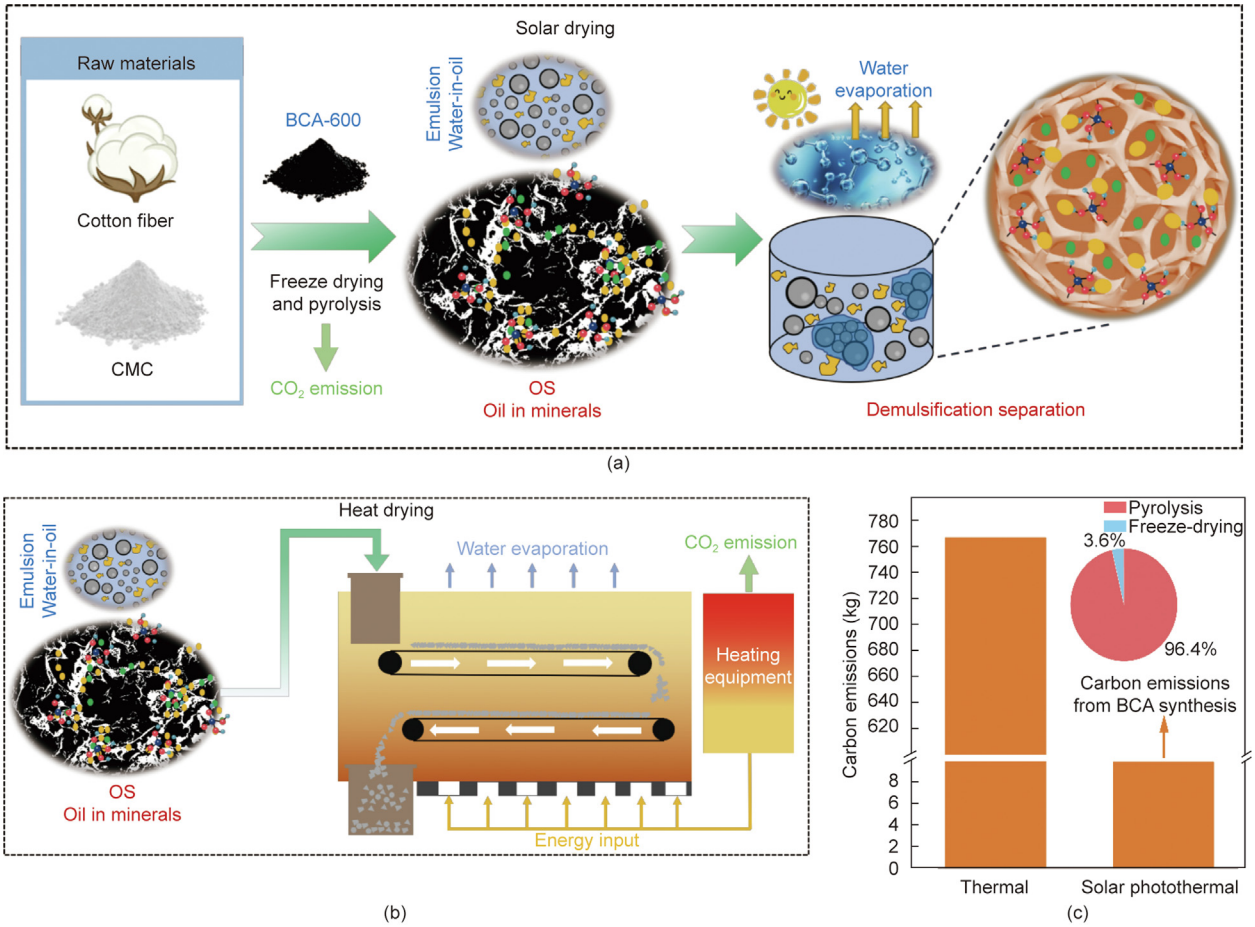

Fig. 9. Schematic diagram of (a) solar photothermal dehydration and (b) traditional thermal dehydration; (c) comparison of carbon emissions between these two methods.

(b) show the main processes of solar photothermal dehydration and traditional thermal dehydration methods. Generally, the carbon emissions of thermal dehydration mainly come from the energy consumption during the process of heating OS by the sludge dryer, while the carbon emissions of solar photothermal dehydration mainly come from the energy consumption in the process of freeze-drying and pyrolysis of BCA-600. The detailed calculation is presented in Text S1 in Appendix A. The OS sample was selected with oil content of 40.0%, water content of 26.7%, and solid content of 33.3%. Fig. 9(c) clearly shows that solar photothermal dehydration significantly reduces carbon emission, which is only 1/100 compared with thermal dehydration. It should be noted that the following utilization of BCA in the pyrolysis process for enhancing heat and mass transfer and more oil recovery was not taken into consideration, which also brought more carbon benefits. Specifically, to achieve dehydration of 1000 of OS and 768.56 kg of CO_2, should be discharged theoretically through the thermal method, in which approximately 87.24% originated from the latent heat of water vaporization. In comparison, the carbon emission from solar photothermal dehydration only originated from BCA synthesis. The freeze-drying and pyrolysis processes accounted for 3.6% and 96.4% of the total carbon emissions respectively, because pyrolysis is an endothermic reaction. However, compared with thermal dehydration, solar photothermal dehydration still faces a certain gap in dehydration efficiency due to site restrictions and natural lighting conditions. Future work should be devoted to developing novel evaporation technology with solar irradiation to overcome the restriction from oil existence. Besides, the technique combination of solar photothermal and traditional thermal dehydration might be a good choice, for which the former can help to reduce the water content and the pressure for following thermal treatment will decline significantly.

Based on the above analysis, the following suggestions for future material design might consider these critical directions. First, the photothermal conversion material needs to have a certain adsorption capacity and emulsion separation capacity. Therefore, the pore structure of the material needs to be able to accommodate a sufficient mass of oil, but at the same time, the pore size is not too large to effectively separate the emulsion. The submicron to micron level of aperture is more appropriate. Secondly, although it is simple and convenient to obtain the photothermal conversion ability through carbonized materials, heat treatment often destroys the structure and surface functional groups of the materials themselves to a certain extent, such as the decrease of adsorption capacity caused by pore collapse and the decrease of co-pyrolysis catalytic effect caused by the reduction of oxygen-containing functional groups. Therefore, it is feasible to consider other methods to make the material obtain the photothermal conversion ability, such as surface modification. Finally, evaporation of OS leads to the spill of VOCs and heavy metals, and considering materials with selective adsorption or degradation will contribute to the low pollution emissions of the process.

4. Conclusions

This study proposes the solar-driven photothermal conversion technology for efficient dehydration of OS and purification of oily water with a multifunctional biomass-based carbon aerogel,

derived from CMC and cotton fiber. The carbon aerogel, BCA-600, possessed abundant pore structure and excellent photothermal conversion effect. It achieved superior oil–water selective wettability through simple surface engineering, contributing to the application potential for oil–water separation by demulsification. Reported efficiencies include 97.28% for hexane and 88.81% for diesel water-in-oil emulsions. The photothermal conversion of BCA-600 also reduced oil viscosity during the adsorption of floating crude oil on the water surface under sunlight. Moreover, this biomass-based carbon aerogel is proposed for the first time for OS dehydration using the solar photothermal method. Experimental results demonstrated that adding BCA-600 significantly enhanced dehydration efficiency for both oil–water emulsions and OS. The 10:2 mass ratio of OS with BCA-600 achieved dehydration efficiencies ranging from 73.27% to 90.72% for OS with varied water content. The presence of oil limited the dehydration due to its coating effect on water droplets, which absorb heat and impede heat transfer to water. Conversely, soil presence promoted water evaporation because of its low specific heat capacity and loosen structure for heat mass transfer. The synergistic functions of solar heating, separation–adsorption of oil–water emulsions, photothermal conversion characteristics, and BCA-600 unique pore structure are key factors driving OS dehydration. Notably, BCA-600 could leave in dehydrated OS to participate in the subsequent pyrolysis process, which could reduce the reaction activation energy, and achieve "one stone two birds." Overall, this new method with the assistance of solar energy for oily pollutants treatment significantly reduces carbon emissions compared to the traditional thermal dehydration process and exhibits varied positive effects, which also provides new avenues for future pollutants treatment using renewable energy with a focus on carbon neutrality.

CRediT authorship contribution statement

Fawei Lin: Writing – review & editing, Supervision, Resources, Conceptualization. **Hongyun Yao:** Writing – original draft, Validation, Methodology, Investigation, Data curation. **Chujun Luan:** Methodology, Data curation. **Chenxu Zhong:** Investigation, Formal analysis, Data curation. **Huiyi Mao:** Data curation. **Lei Che:** . **Hongdi Yu:** Writing – review & editing, Investigation. **Guanyi Chen:** Supervision, Resources, Methodology. **Eslam Salama:** Software. **Mona Ossman:** Formal analysis. **Li'an Hou:** Supervision, Methodology, Funding acquisition.

Declaration of competing interest

The authors declare that they have no known competing financial interests or personal relationships that could have appeared to influence the work reported in this paper.

Acknowledgments

This work was supported by the National Natural Science Foundation of China (52376205) and the Chinese Academy of Engineering Strategic Research and Consulting Project (2023-XZ-38).

Appendix A. Supplementary data

Supplementary data to this article can be found online at https://doi.org/10.1016/j.eng.2025.01.008.

References

[1] Nixon Z, Zengel S, Baker M, Steinhoff M, Fricano G, Rouhani S, et al. Shoreline oiling from the deepwater horizon oil spill. Mar Pollut Bull 2016;107(1):170–8.
[2] Brette F, Machado B, Cros C, Incardona JP, Scholz NL, Block BA. Crude oil impairs cardiac excitation–contraction coupling in fish. Science 2014;343(6172):772–6.
[3] Peterson CH, Rice SD, Short JW, Esler D, Bodkin JL, Ballachey BE, et al. Long-term ecosystem response to the Exxon Valdez oil spill. Science 2003;302(5653):2082–6.
[4] Sun AQ, Hou XA, Hu XG. Super-performance photothermal conversion of 3D macrostructure graphene-CuFeSe aerogel contributes to durable and fast clean-up of highly viscous crude oil in seawater. Nano Energy 2020;70:104511.
[5] Ge J, Shi LA, Wang YC, Zhao HY, Yao HB, Zhu YB, et al. Joule-heated graphene-wrapped sponge enables fast clean-up of viscous crude-oil spill. Nat Nanotechnol 2017;12(5):434–40.
[6] Kuang YD, Chen CJ, Chen G, Pei Y, Pastel G, Jia C, et al. Bioinspired solar-heated carbon absorbent for efficient cleanup of highly viscous crude oil. Adv Funct Mater 2019;29(16):1900162.
[7] Ding SQ, Han XH, Zhu LJ, Hu HY, Fan LW, Wang SR. Cleanup of oils and organic solvents from contaminated water by biomass-based aerogel with adjustable compression elasticity. Water Res 2023;232:119684.
[8] Wu SW, Jian RD, Tian SY, Zhou L, Luo TF, Xiong GP. Simultaneous solar-driven seawater desalination and continuous oil recovery. Nano Energy 2023;107:108160.
[9] Gao MM, Peh CK, Phan HT, Zhu LL, Ho GW. Solar absorber gel: localized macro-nano heat channeling for efficient plasmonic Au nanoflowers photothermic vaporization and triboelectric generation. Adv Energy Mater 2018;8(25):1800711.
[10] Ye MM, Jia J, Wu ZJ, Qian CX, Chen R, O'Brien PG, et al. Synthesis of black TiO_x nanoparticles by Mg reduction of TiO_2 nanocrystals and their application for solar water evaporation. Adv Energy Mater 2017;7(4):1601811.
[11] Huang J, He YR, Chen MJ, Wang XZ. Separating photo-thermal conversion and steam generation process for evaporation enhancement using a solar absorber. Appl Energy 2019;236:244–52.
[12] Wang YC, Wang CZ, Song XJ, Megarajan SK, Jiang HQ. A facile nanocomposite strategy to fabricate a rGO-MWCNT photothermal layer for efficient water evaporation. J Mater Chem A 2018;6(3):963–71.
[13] Miao J, Lv FY, Gulfam R, Zhao WP. Synergistic effect of superhydrophilic skeleton decorated with hierarchical micro/nanostructures and graphene oxide on solar evaporation. Appl Energy 2023;350:121779.
[14] Peng B, Yao Z, Wang X, Crombeen M, Sweeney DG, Tam KC. Cellulose-based materials in wastewater treatment of petroleum industry. Green Energy Environ 2020;5(1):37–49.
[15] Lee J, Kim K, Park SH, Yoon GY, Kim J, Lee SJ. Macroporous photothermal bilayer evaporator for highly efficient and self-cleaning solar desalination. Nano Energy 2020;77:105130.
[16] Jin HC, Lin GP, Bai LZ, Zeiny A, Wen DS. Steam generation in a nanoparticle-based solar receiver. Nano Energy 2016;28:397–406.
[17] Ni G, Miljkovic N, Ghasemi H, Huang XP, Boriskina SV, Lin CT, et al. Volumetric solar heating of nanofluids for direct vapor generation. Nano Energy 2015;17:290–301.
[18] Bi HC, Yin ZY, Cao XH, Xie X, Tan CL, Huang X, et al. Carbon fiber aerogel made from raw cotton: a novel, efficient and recyclable sorbent for oils and organic solvents. Adv Mater 2013;25(41):5916–21.
[19] Xu X, Dong FH, Yang XX, Liu H, Guo LZ, Qian YH, et al. Preparation and characterization of cellulose grafted with epoxidized soybean oil aerogels for oil-absorbing materials. J Agric Food Chem 2019;67(2):637–43.
[20] Yue XJ, Zhang T, Yang DY, Qiu FX, Li ZD. Hybrid aerogels derived from banana peel and waste paper for efficient oil absorption and emulsion separation. J Clean Prod 2018;199:411–9.
[21] Li ZX, Lei SJ, Xi JC, Ye DL, Hu WZ, Song L, et al. Bio-based multifunctional carbon aerogels from sugarcane residue for organic solvents adsorption and solar-thermal-driven oil removal. Chem Eng J 2021;426:129580.
[22] Edeh IG, Masek O, Fusseis F. 4D structural changes and pore network model of biomass during pyrolysis. Sci Rep 2023;13(1):22863.
[23] Hyväluoma J, Hannula M, Arstila K, Wang HL, Kulju S, Rasa K. Effects of pyrolysis temperature on the hydrologically relevant porosity of willow biochar. J Anal Appl Pyrolysis 2018;134:446–53.
[24] Shaaban A, Se SM, Dimin MF, Juoi JM, Mohd Husin MH, Mitan NMM. Influence of heating temperature and holding time on biochars derived from rubber wood sawdust via slow pyrolysis. J Anal Appl Pyrolysis 2014;107:31–9.
[25] Congsomjit D, Areeprasert C. Hydrochar-derived activated carbon from sugar cane bagasse employing hydrothermal carbonization and steam activation for syrup decolorization. Biomass Convers Biorefin 2021;11(6):2569–84.
[26] Coasne B. Multiscale adsorption and transport in hierarchical porous materials. New J Chem 2016;40(5):4078–94.
[27] Wang ZD, Xiao CM, Wu ZJ, Wang YT, Du X, Kong W, et al. A novel 3D porous modified material with cage-like structure: fabrication and its demulsification effect for efficient oil/water separation. J Mater Chem A 2017;5(12):5895–904.
[28] Sutar RS, Wu XN, Latthe SS, Shi BR, Xing RM, Liu SH. Efficient separation of oil–water emulsions: competent design of superwetting materials for practical applications. J Environ Chem Eng 2023;11(6):111299.
[29] Yu TL, Halouane F, Mathias D, Barras A, Wang ZW, Lv AQ, et al. Preparation of magnetic, superhydrophobic/superoleophilic polyurethane sponge: separation of oil/water mixture and demulsification. Chem Eng J 2020;384:123339.
[30] Li LX, Li BC, Sun HX, Zhang JP. Compressible and conductive carbon aerogels from waste paper with exceptional performance for oil/water separation. J Mater Chem A Mater Energy Sustain 2017;5(28):14858–64.

[31] Chen ZB, Zhan B, Li SY, Wei DS, Zhou WT, Liu Y. Facile fabrication of corn stover-based aerogel for oil/water separation. Separ Purif Tech 2022;298:121642.
[32] Tian JS, Zhang T, Talifu D, Abulizi A, Ji YJ. Porous carbon materials derived from waste cotton stalk with ultra-high surface area for high performance supercapacitors. Mater Res Bull 2021;143:111457.
[33] Wang CL, Ma D, Bao XH. Transformation of biomass into porous graphitic carbon nanostructures by microwave irradiation. J Phys Chem C 2008;112 (45):17596–602.
[34] Zhao CX, Huang HR, Li ZY, Li JX, Li YT, Xiang D, et al. 3D superhydrophobic/superoleophilic sponge with hierarchical porous structure and robust stability for high-efficiency and continuous separation of oily wastewater. Separ Purif Tech 2022;299:121820.
[35] Shi CC, Wang TQ, Roy S, Chopra SS, Chen GX, Shang J, et al. From waste to resource: surface-engineered spent coffee grounds as a sustainable adsorbent for oil–water separation. Acs Est Eng 2023;3(9):1297–307.
[36] Yang JB, Wang HC, Tao ZA, Liu XP, Wang ZW, Yue RR, et al. 3D superhydrophobic sponge with a novel compression strategy for effective water-in-oil emulsion separation and its separation mechanism. Chem Eng J 2019;359:149–58.
[37] Shi L, Shi Y, Zhuo SF, Zhang CL, Aldrees Y, Aleid S, et al. Multi-functional 3D honeycomb ceramic plate for clean water production by heterogeneous photo-Fenton reaction and solar-driven water evaporation. Nano Energy 2019;60:222–30.
[38] Li JT, Lin FW, Yu HD, Tong X, Cheng ZJ, Yan BB, et al. Biochar-assisted catalytic pyrolysis of oily sludge to attain harmless disposal and residue utilization for soil reclamation. Environ Sci Technol 2023;57(17):7063–73.
[39] Chen W, Fang Y, Li KX, Chen ZQ, Xia MW, Gong M, et al. Bamboo wastes catalytic pyrolysis with N-doped biochar catalyst for phenols products. Appl Energy 2020;260:114242.
[40] Ren SJ, Lei HW, Wang L, Bu Q, Chen SL, Wu J. Hydrocarbon and hydrogen-rich syngas production by biomass catalytic pyrolysis and bio-oil upgrading over biochar catalysts. Rsc Adv 2014;4(21):10731–7.
[41] Lin FW, Yu HD, Li JT, Zygourakis K, Li RD, Cheng ZJ, et al. Investigation on the interaction between oil compositions and soil minerals with the targets of resource recovery and harmless disposal of oily sludges by pyrolysis. Acs Est Eng 2023;3(5):734–44.
[42] Li JT, Zheng F, Li QS, Farooq MZ, Lin FW, Yuan DK, et al. Effects of inherent minerals on oily sludge pyrolysis: kinetics, products, and secondary pollutants. Chem Eng J 2022;431:133218.